

Design and Linearity Assessment of the TRISTAN Detectors' Remote Analog to Digital Conversion DAQ System

A.S. Gavin,^{a,b,1} M. Balzer,^c S. Chilingaryan,^c R. Henning,^{a,b} A. Kopmann,^c S. Mertens,^d J. Mostafa,^c A. Onillon,^d F. Simon,^c N. Tan Jerome,^c D. Tcherniakhovski,^c K. Urban,^e J. F. Wilkerson,^{a,b} S. Wüstling^c

^a*Department of Physics and Astronomy, University of North Carolina, Chapel Hill, NC 27599, U.S.A.*

^b*Triangle Universities Nuclear Laboratory, Durham, NC 27708, U.S.A.*

^c*Institute for Data Processing and Electronics (IPE), Karlsruhe Institute of Technology (KIT), Hermann-von-Helmholtz-Platz 1, 76344 Eggenstein-Leopoldshafen, Germany*

^d*Max-Planck-Institut für Kernphysik, Saupfercheckweg 1, 69117 Heidelberg, Germany*

^e*Department of Physics, TUM School of Natural Sciences, Technical University of Munich, James-Franck-Straße 1, 85748 Garching b. München, Germany*

E-mail: andrew.gavin@mpi-hd.mpg.de

ABSTRACT: The TRISTAN detector is an upgrade to the KATRIN experiment to enable a differential measurement of the tritium β -decay spectrum to search for the experimental signature of keV scale sterile neutrinos. The TRISTAN detector upgrade consists of performing precision electron spectroscopy with over 1000 silicon drift detector pixels, each responsible for recording event rates of 10^5 counts per second. A project specific data acquisition (DAQ) system is developed to meet the experimental challenges with a remote analog to digital conversion (RADC) design. In this work, the conceptual design of the RADC DAQ is presented along with the built system for operating the TRISTAN detector upgrade. The system includes flexible signal processing logic and data management that is optimized for the high-rate precision measurement. The non-linearity of the system's readout channels are measured and shown to be stable over time. The systematic effect of this non-linearity is propagated to the sensitivity to the sterile neutrino signature and is demonstrated to be reducible to a subdominant contribution.

KEYWORDS: data acquisition concepts, digital signal processing, data processing methods, trigger algorithms

¹Present address: Max-Planck-Institut für Kernphysik, Saupfercheckweg 1, 69117 Heidelberg, Germany

Contents

1	Sterile Neutrino Search with the TRISTAN Detector Upgrade	1
2	Remote Analog to Digital Conversion Concept	2
3	Front-End DAQ System	3
4	Back-End DAQ System	6
5	Readout Non-Linearity Measurement	9
6	Sterile Neutrino Sensitivity	11
7	Conclusion	14

1 Sterile Neutrino Search with the TRISTAN Detector Upgrade

A natural extension to the Standard Model is the addition of right-handed counterparts to the observed left-handed neutrinos. These neutrinos would be neutral under the weak interaction and therefore have Majorana masses that are independent of the electroweak symmetry breaking scale [1]. They are commonly called sterile neutrinos, as they would only interact gravitationally and through their mixing to the active neutrinos. Light sterile neutrinos, with eV scale masses, have been proposed as partial solutions to existing experimental neutrino anomalies [2]. At the keV mass scale, sterile neutrinos are proposed as a viable candidate for part of the dark matter [3, 4].

Determination of neutrino properties through precision measurements of β -decays is possible due to the impact of the neutrino mass eigenstates in decay kinematics. The differential decay rate, $d\Gamma/dE$, is sensitive to the effective neutrino mass, m_ν , when the individual mass eigenstates have small mass differences. Shape distortions at the endpoint of the tritium β -decay spectrum are measured by the Karlsruhe Tritium Neutrino (KATRIN) experiment to place leading limits on the effective active neutrino mass [5, 6].

The existence of a sterile neutrino introduces an additional mixing branch to the produced electron anti-neutrino, which modifies the differential decay rate to $d\Gamma/dE = \cos^2(\theta)d\Gamma(m_\nu)/dE + \sin^2(\theta)d\Gamma(m_4)/dE$. The additional sterile branch is parameterized by the sterile neutrino mass, m_4 , and mixing angle between the sterile and active states, $\sin^2(\theta)$. The superposition of these two distinct decay branches would produce a kink-like distortion in the decay spectrum.

Searches for a kink-like distortion in the KATRIN neutrino mass data have led to competitive limits on eV scale sterile neutrinos [7]. During the commissioning phase of the KATRIN experiment, the tritium spectrum was measured over a wider energy range, the analysis of this data gives limits of $\sin^2 \theta < 5 \cdot 10^{-4}$ (95% C.L.) for a sterile neutrino with $m_4 = 1 \text{ keV}$ [8]. Constraining sterile neutrino mixing at higher masses and lower mixing requires a wider energy measurement range

and better statistical scaling with measurement time. The upcoming TRISTAN detector upgrade to the KATRIN experiment is designed to perform a high precision differential measurement of the full tritium spectrum, with a goal of improving the statistical sensitivity to keV sterile neutrinos to mixing of $\sin^2 < 10^{-6}$ (95% C.L.) [9].

A highly pixelated silicon drift detector (SDD) array was chosen for this application and built at the Semiconductor Laboratory (HLL) of the Max Planck Society. A TRISTAN detector module is composed of a monolithic array of 166 hexagonally tessellated 7 mm^2 pixels. One pixel is designed to operate at $\mathcal{O}(100\text{ kcps})$ and have an energy resolution of 250 eV for 20 keV electrons. An installation of nine modules, totaling 1494 pixels, in the KATRIN detector section is planned for the keV sterile neutrino search [9]. In this work the novel remote analog to digital conversion (RADC) data acquisition (DAQ) system is presented as a robust and scalable readout and operational architecture for the TRISTAN detector upgrade.

2 Remote Analog to Digital Conversion Concept

The DAQ system of the TRISTAN detector modules must provide low distortion digitization and event filtering for a large number of pixels operating at high rates. Its structure is based on early signal digitization by front-end boards and subsequent signal processing on back-end field-programmable gate array (FPGA) boards. The design concept of this custom remote analog to digital conversion (RADC) DAQ is shown in Figure 1.

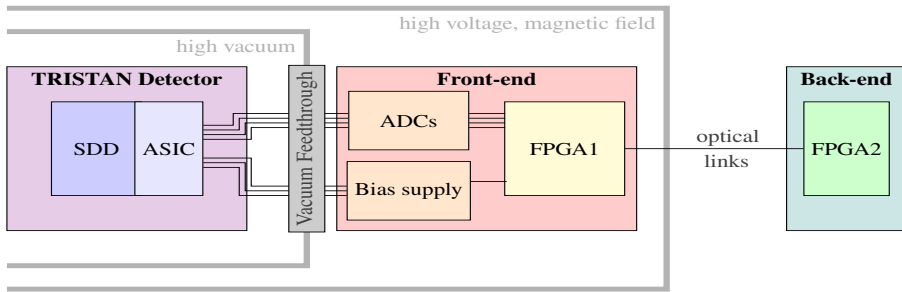


Figure 1. Concept of an RADC DAQ system operating in the KATRIN detector section. Environmental constraints from the high voltage and magnetic field are outlined in gray and isolated to the front-end board which provides detector bias voltages and digitizes the detector signals with minimized analog paths. Connection via optical links to a back-end unit allows for flexible event filtering and readout mode implementation.

The minimization of analog signal paths is desired to decrease the coupling of electronics noise into the detector waveforms, which decrease the energy resolution of the TRISTAN detector. Therefore, the front-end board is mounted directly on the vacuum chamber and is designed to be operated in a strong magnetic field and insulated from high-voltage. The front-end board digitizes and packetizes the detector waveforms, which are sent via high-speed fiberoptic data links to the back-end FPGA boards, which are located outside of the stray magnetic fields of the detector magnet and on earth ground potential.

Waveform signals are then processed through digital signal processing architectures and event creation logic implemented on the FPGA. Digital signal filtering creates events from detector pulses with the associated timing and energy evaluations, charge sharing and pileup flagging, and

other desired pulse attributes. Data from the back-end is processed through a high-performance Ethernet-based DAQ system that interfaces with the computer server and data storage.

The separation of the two stages allows for the development of project specific front-end boards that meet the operational design requirements of integrating the TRISTAN detector into the KATRIN detector section. Removing these design requirements from the back-end allows the use of more standardized FPGA boards that provide flexible signal processing without a completely new development.

3 Front-End DAQ System

The primary component of the front-end DAQ system is the Tile Main Board (TMB); a project specific board designed by the KIT Institute for Data Processing and Electronics (IPE). Each TMB is designed to digitize and transmit detector signals and provide slow control for a single 166-pixel detector module.

A TRISTAN detector module consists of a monolithic silicon SDD chip attached perpendicularly to a copper cooling and support structure, which hosts the in-vacuum electronic readout components [10]. Signal amplification and detector control is provided by the ETTORE ASIC, which is a 12-channel low-noise charge sensitive amplifier with a pulsed reset tailored to operate with the TRISTAN SDD with an integrated junction field-effect transistor [11]. Each module is equipped with two high-density ASIC boards containing seven ASICs each. The amplified detector signals are driven through $O(1\text{ m})$ Kapton flat cables to the vacuum feedthroughs.

Each TMB is connected onto the detector vacuum chamber by four 100-pin micro-D connectors, providing connections for detector signal readout, in-vacuum sensor readout, and in-vacuum electronic control voltages. The location at the detector chamber sits on a high voltage of up to 25 kV, necessary for the operation of a post-acceleration electrode (PAE), and is exposed to a $O(100\text{ mT})$ stray magnetic field of the detector magnet. [12]. Therefore, the TMB excludes any ferromagnetic components and is powered with isolation transformers. All data transfer between a TMB and the back-end FPGA board is done via fiberoptic links.

The TMB consists of a $411\text{ mm} \times 340\text{ mm}$ PCB that is populated with submodules, each with a specific readout or control task. The separation of tasks into smaller submodules allows for easier development, troubleshooting, and repair. The TMB sub modules include: Microcontroller (μC), Power Supply, Bias, RESET, voltage offset or Gatti Slider, and ADC Boards. The components and connections of the TMB's submodules are diagrammed in [Figure 2](#), with an example TMB installed on a detector chamber shown in [Figure 3](#).

The control of the TMB operation and slow control readout is performed over a 1 Gb/s QSFP ethernet connection. An OpenIPMC μC Board distributes the slow control parameters to their respective submodules, the Bias Supply, Gatti Slider Boards, and Power Supply Board [13]. Readout of temperature sensors on the detector and ASIC are also processed through the μC Board.

All components of the TMB are powered through a Power Supply Board that is fed with a supply voltage of 12 V and a supply current of 15 A. Air-coil DC/DC converters are used to derive the necessary voltages for operating each of the TMB submodules and FPGAs.

The bias and supply voltages necessary for operating the SDDs are communicated from the μC Board to the Bias Board. The Bias Board consists of 10 digital to analog converters, which supply

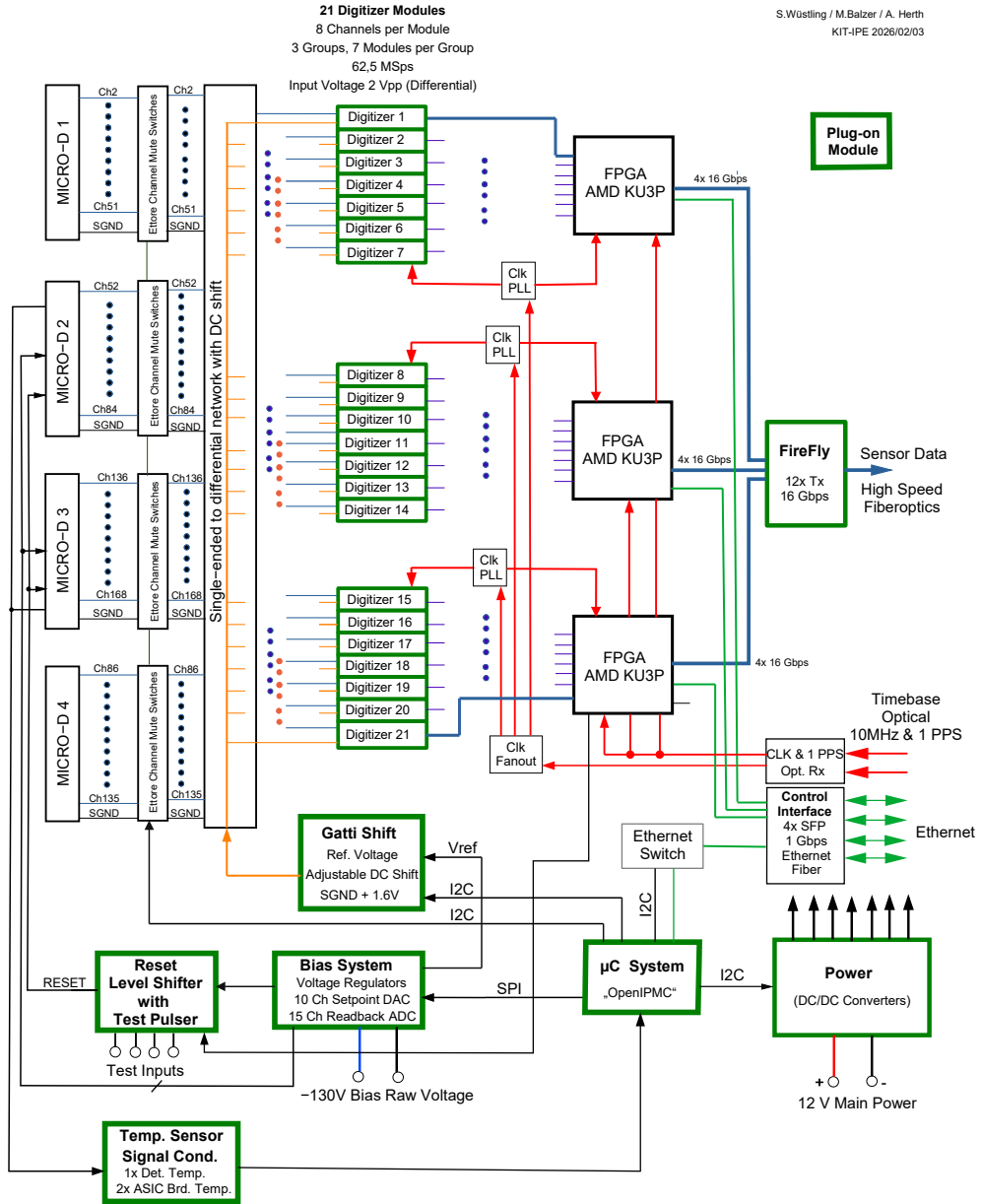


Figure 2. Block diagram of the Tile Main Board (TMB). Green blocks indicate individual plug-on sub modules which populate the PCB. The TMB provides detector operating voltage and waveform readout through the four micro-D connectors and streams waveform data to the backend through fiberoptic transceivers.

the necessary voltages to the middle two micro-D vacuum feedthroughs. A 15 channel ADC is also implemented for real time slow control readback of the detector operating voltages.

A reference voltage for applying a DC-offset to the detector signals before digitization is provided by the Gatti Slider Board. The offset is necessary to map the voltage output of the detector into the operating range of the ADC boards. The offset value is set in the slow control parameters and

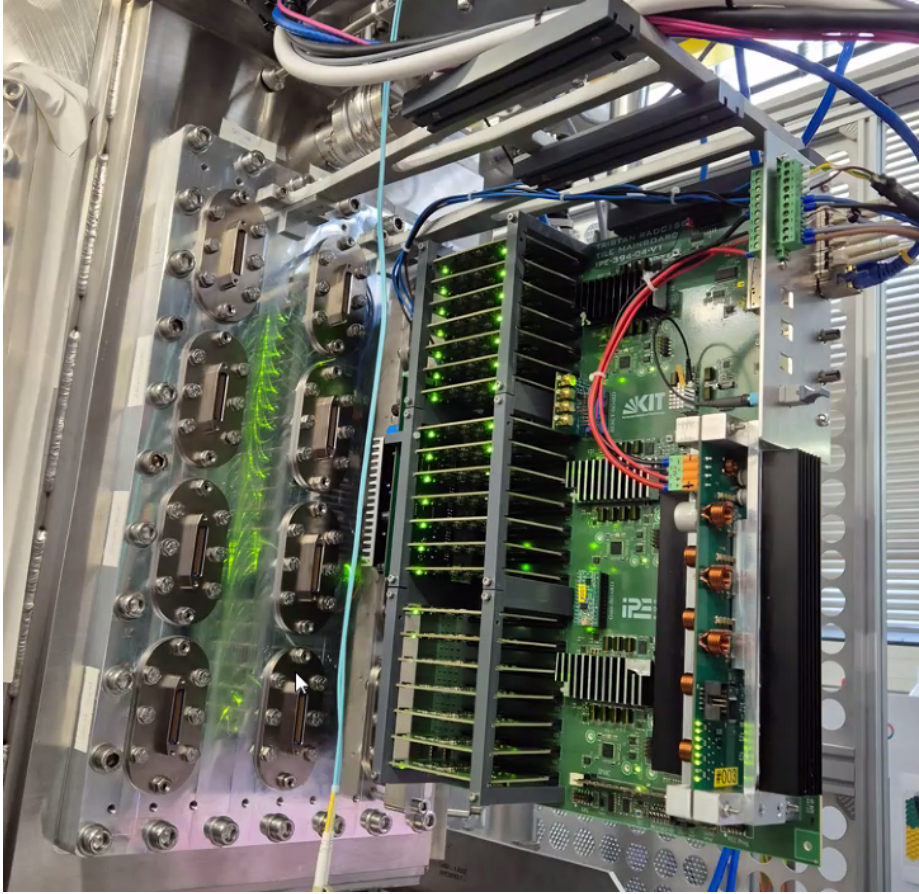


Figure 3. Tile Main Board (TMB) installed and operated at a replica of the detector chamber upgrade. 21 ADC cards are mounted perpendicular to the TMB to allow for dense PCB design. Fiber optic connections on the right side provide connections to back-end control and readout. Two mounting positions for additional TMBs are visible to the left; each a column of four micro-D vacuum feedthroughs.

is changed between measurements to randomize the pulse positions within the digitization range. The addition of this board was necessitated by investigations of the impact of ADC non-linearities on event energy reconstruction, which are discussed in [Section 5](#). A voltage stability of < 0.1 mV is necessary over the digitization of individual detector pulses to not introduce substantial bias to the energy reconstruction.

Each TMB is equipped with three FPGAs, which control the processing and transfer of detector waveforms. One FPGA additionally controls the RESET Board to provide periodic detector resets. The signal readout is inhibited in the ETTOREs and the detector anodes are discharged to return to a nominal operating point during each reset. The RESET board also allows for injection of test signals from an outside signal source to the readout chain.

Readout of the analog signals from a 166-pixel detector is performed by 21 ADC Boards and three FPGAs. Slow control parameters for the sampling frequency and downsampling ratio are set in the FPGAs via the SFP module’s 1 Gb/s ethernet connection.

Each ADC Board is composed of an anti-aliasing filter and an 8-channel AD9257 ADC.¹ A 5th order Bessel low-pass filter is used due to it being well suited for pulse processing [14]. The AD9257 provides 14-bit sampling of the detector signals in a 2 V_{pp} range at a sampling frequency of up to 65 MHz. Each ADC Board streams data at a rate of 6.78 Gb/s to the FPGA.

An additional bit of information is added in the FPGA per sample indicating whether an inhibit signal is present, either from the RESET Board or from an external input. The front end FPGAs serialize, packetize, and format the data from the ADC Boards for fiber optic transmission. The streaming of data from the FPGAs to the back-end is performed by 12 Samtec FireFly™ optical transceivers. Each transceiver operates at up to 16 Gb/s, providing an overall streaming rate of 192 Gb/s in order to directly stream all 168 channels.

Time synchronization between components within one TMB, multiple TMBs, and the back-end system is controlled by a master GPS clock. The GPS clock provides 1 Hz and 10 MHz signals via fiber optic lines to synchronize the DAQ system. Within a single TMB, the 10 MHz master clock signal is used to synchronize the ADC and DC/DC converters to avoid forming beat frequencies.

4 Back-End DAQ System

Transmission via fiberoptic cables allows the back-end system to be located outside of the stray magnetic fields and off the post-acceleration high voltage of the detector chamber, lifting the environmental design requirements needed for the front-end board from the back-end system. The function of the back-end system is to provide multiple readout modes of TRISTAN detector data through digital signal processing and event creation.

The hardware platform for the back-end system is the Serenity-S1 FPGA ATCA-card developed by KIT-IPE and CMS-collaborators for the CMS detector at the LHC [15, 16]. Serenity-S1 cards are stored in ATCA racks and provide the detector signal processing through an AMD Virtex UltraScale+ FPGA.² The VU9P version is used in the context of the TRISTAN DAQ. Each Serenity-S1 card is capable of processing the data from three TMBs, providing the readout of 498 TRISTAN detector pixels. Digital signal processing on the FPGA allows for the implementation of tailored filtering algorithms for the transmitted waveforms.

Four readout modes; Waveform, ListWave, ListMode, and Histogram, are implemented in the back-end processing. Waveform readout directly saves all data streamed from the front-end. ListWave and ListMode readouts record triggered detector events with and without an associated waveform snippet, respectively. Histogram readout populates predefined energy histograms with the triggered events based on decision tree logic. While science data taking will primarily be taken using the Histogram readout, the other readout modes enable systematic studies of detector and data processing related effects.

Events in the TRISTAN detector create electric pulses with a fast risetime, $\tau_{\text{rise}} \sim \mathcal{O}(10 \text{ ns})$, and subsequent decaying tail, with a decay constant of $\tau_{\text{decay}} \sim \mathcal{O}(10 \mu\text{s})$. A combination of two filters, a fast trigger filter and an energy filter, are used to have optimized performance in both event energy reconstruction and event pileup rejection. The response of the trigger and energy filter to a delta impulse and a detector event waveform are displayed in Figure 4.

¹<https://www.analog.com/en/products/ad9257.html>

²<https://docs.amd.com/r/en-US/ds923-virtex-ultrascale-plus/>

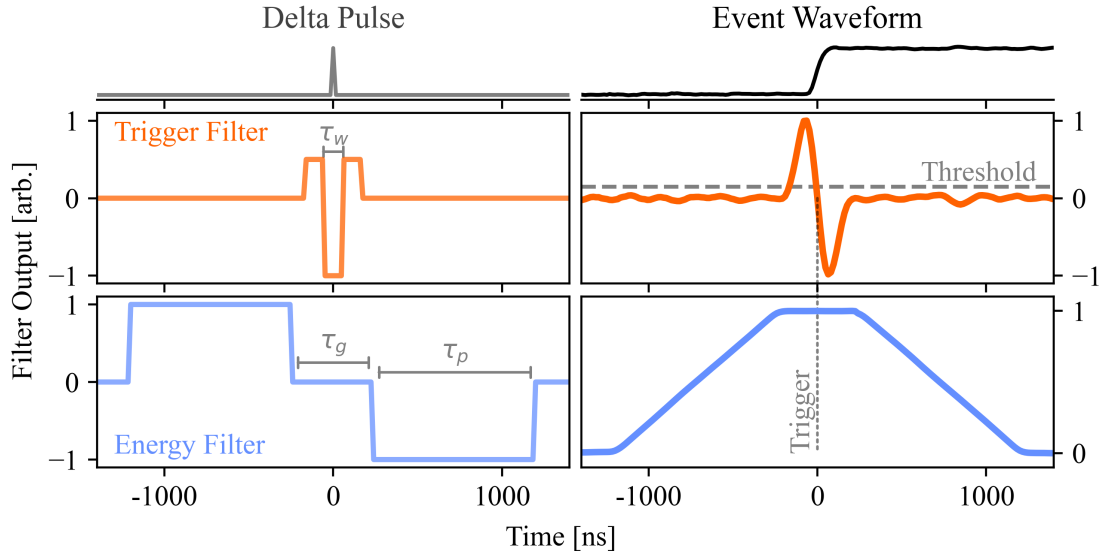


Figure 4. Example response of the trigger (top) and energy (bottom) filters to delta pulse and detector event waveforms. The filters are parameterized by widths τ_w , τ_g , and τ_p . An event trigger is produced and the energy filter is evaluated at the first zero crossing of the trigger filter after a threshold crossing.

A fast filter is used to trigger the readout of a detector event and distinguish between coincident events within the detector. The trigger filter is based on a triangular filter, with time width τ_w , adjustable within the range of 64 ns to 1 μ s. The response to an event occurring within the detector pixel is a heartbeat-like signal, the amplitude of which corresponds to the pulse height. The trigger filter is set to an armed state after crossing a fixed threshold value, and a trigger is produced for the time stamp corresponding to the next zero crossing.

Both τ_w and the threshold are optimized for each pixel and set independently. The response length of the trigger filter is proportional to τ_w , and therefore a minimization of this length is useful to distinguish between coincident detector events. However, τ_w must remain longer than the detector risetime τ_{rise} to produce the necessary heartbeat response. The threshold is set to optimize the triggering efficiency for low energy detector events while not introducing large contributions of noise triggers. Typical operating parameters result in better than 99% trigger efficiency for detector events with 2 keV energy depositions. The event time stamp from the trigger filter benefits from being independent of event energy, unlike a pure threshold trigger applied to a trapezoidal filter.

The energy of a triggered event is reconstructed using pulse height analysis by an energy filter, which consists of an exponential deconvolution and a trapezoidal filter. A digital offset is applied to the waveform to correct for the detector working point voltage and analog Gatti offset. An exponential deconvolution is then applied with a decay constant of τ_d , which removes the decaying tail of the waveform to produce a step-like pulse. This provides a more stable response for the energy evaluation of the trapezoidal filter. The offset value and τ_d are independently controlled for each detector channel and set by measurements taken in Waveform mode.

The energy filter is a trapezoidal filter with shaping time, τ_p , and gap time, τ_g , parameters. Energy filtering of a detector event results in a trapezoidal response with side widths corresponding

to τ_p and a flat top width corresponding to τ_g . These parameters are individually adjustable within the ranges of 64 ns to 8 μ s, and 0 ns to 1024 ns, respectively. Both parameters are optimized to meet the energy resolution and filter stability requirements while minimizing the impact of event pileup on the measured electron energy spectrum.

An event builder takes event triggers and produces triggered event information packets which are saved in ListWave and ListMode readout modes. Each event packet consists of a header with 32 bytes of information: an 8 byte timestamp, 4 byte energy evaluation, 2 byte channel number, 2 byte flag, and 16 bytes of additional waveform information that can be flexibly implemented by the user. In ListMode readout a list of events is saved, while in ListWave a snippet of the triggered waveform is also saved for each event. The length of the saved waveform is adjustable up to $\mathcal{O}(10 \mu\text{s})$ in order to fully sample the rising edge and decaying tail of the detector waveform.

Measurement at high rates lead to pileup contributions of $\mathcal{O}(10\%)$ to the measured spectrum and therefore must be accurately flagged by the filter logic. Coincident events occurring within a pixel bias the energy reconstruction logic if the resulting energy filters overlap and are flagged for events occurring within a pileup window, w_{pu} , of another event. These events can be excluded from analyses to avoid this bias and are considered resolved pileup events. Coincident events within $\lesssim \tau_w$ produce a variable number of triggers depending on the event energies and time separations. A trigger holdoff, w_h , is applied which inhibits the creation of multiple triggers within a given time window. These events are indistinguishable from single energy depositions in the filtering algorithm and remain in the measured spectrum as unresolved pileup. Event triggers are shared between readout channels within the same Serenity-S1 card through versatile trigger distribution maps. Maps of physically neighboring pixels allows the flagging of coincident events that could be biased by charge sharing near the pixel borders. Events that are biased by other inter-pixel effects, such as crosstalk between readout lines, can also be flagged by dedicated maps built from characterization measurements. Events affected by detector saturation, detector reset periods, or other waveform distortions are also flagged. An additional 16 bytes is available for configuration to save any waveform parameter of interest.

In Histogram readout mode the events from ListMode are used to populate histograms corresponding to their energy evaluation, channel number, and flags. Production of multiple histograms from the same data, incorporating different flag combinations, allows for the systematic study of different effects on the measured energy spectrum. The dynamic range of the energy histograms, as well as the energy resolution of each histogram bin, is set by the user. The analysis of the full tritium spectrum will utilize data produced by an optimized set of histogram parameters and flags to minimize systematic effects.

The rate of data produced while operating the TRISTAN DAQ is dependent on the selected readout mode. Operation of the Waveform readout produces data at a rate of 125 MB/s per pixel, which results in an overall data rate of 186.7 GB/s for nine modules. A reduction in data rate is obtained in the ListMode readout for . Recording 100 kcps per pixel in a ListMode readout produces a data rate of 3.2 MB/s per pixel, or only 4.78 GB/s for nine modules. However, for a measurement campaign of four months this still corresponds to $\mathcal{O}(10 \text{ PB})$ of saved data. The largest reduction in the size of data produced comes from the Histogram readout. Filling histograms with eV scale energy resolutions and minute scale timing intervals reduces the overall amount of produced data to $\mathcal{O}(10 \text{ TB})$ for a four month campaign.

Further processing and storage is performed by an enterprise-grade computer server after receiving data from the backend Serenity-S1 boards. The Serenity-S1 board runs a resource-efficient implementation of the Ethernet data transfer protocols: User Datagram Protocol (UDP), Internet Protocol version 4 (IPv4) over MAC & PMA/PCS Xilinx IP core. The implementation utilizes only 1,048 configurable logic blocks (CLBs) of the available 67,200 CLBs (roughly 1.5%) and zero Block RAM resources. The backend Serenity-S1 boards encapsulate the detector events in UDP packets and sends them to the enterprise-grade computer server over the 100 Gbps Ethernet links.

On the DAQ computer server, we run software-based logic for data processing and storage. A challenging part of this logic is handling the possible hundreds of Gb/s from the Serenity-S1 boards with zero data loss. To overcome this challenge, we exploit the Data Acquisition Development Kit (DQDK), a software framework for high-performance Ethernet-based data acquisition [17]. The framework uses an emerging high-performance networking technology capable of handling hundreds of Gb/s. In addition, software optimizations and computer architectural support enhance performance through parallelism and overcome possible memory bottlenecks [18]. For the Waveform and ListWave modes, the DQDK framework receives the data from the Serenity-S1 boards and then copies it to a larger intermediate buffer before saving it at the end of the session. However, for the ListMode and the Histogram modes, the DQDK framework constructs an energy histogram in memory based on the received events.

5 Readout Non-Linearity Measurement

A fundamental metric of the performance of the DAQ system is its linear response to input voltages, which is primarily determined by the performance of the ADC. An ADC maps a voltage input range onto the number of digital bins of the digitizer. In an ideal ADC, the voltage range corresponding to each bit are of equal size and the digitization only introduces quantization error. In practice, ADCs exhibit non-linear effects due to their electrical architectures and input voltages are not perfectly mapped to digital bins [19].

The difference between an ADC's performance and the ideal can be parameterized by its differential non-linearity (DNL). The DNL is a measure of the deviation of a single ADC voltage bin width to the average. For an N -bit digitizer with a total voltage input range of ΔV , the DNL of the i^{th} ADC code is expressed as

$$\text{DNL}_i = \Delta V_i / (\Delta V / 2^N) - 1, \quad (5.1)$$

where ΔV_i is the voltage range mapped onto that ADC code. The DNL can be directly measured by comparing the histogram of recorded values in each ADC bin to the predicted distribution for a known input signal [20, 21]. Linear ramp signals, which produce an equal probability of measurement in all ADC bins, were used to test the differential non-linearity of the readout channels.

The primary measurements of this study were performed with a Rohde & Schwarz UPV Audio Analyzer producing a slow triangular waveform.³ The voltage amplitude was tuned to cover the full

³<https://www.rohde-schwarz.com/de/broschuere-datenblatt/upv/>

dynamic range of the ADC and the triangular wave was used to reduce biases from hysteresis. Five ADC cards were tested, with a 16 s measurement performed for each channel. This measurement time was chosen to reach a statistical uncertainty of 4×10^{-3} through the accumulation of 10^9 samples in the 14-bit digitizer.

The calculated DNL of a single channel is shown for an 8-bit range of the ADC in [Figure 5 \(a\)](#). The DNL consists of a comb-like structure of ≈ 0.5 lsb spikes with 5-bit separations and background noise fluctuations on the scale of $\sigma = 0.026$ lsb. These results match the specifications provided by Analog Devices for the typical non-linearity performance of the AD9257 ADC.

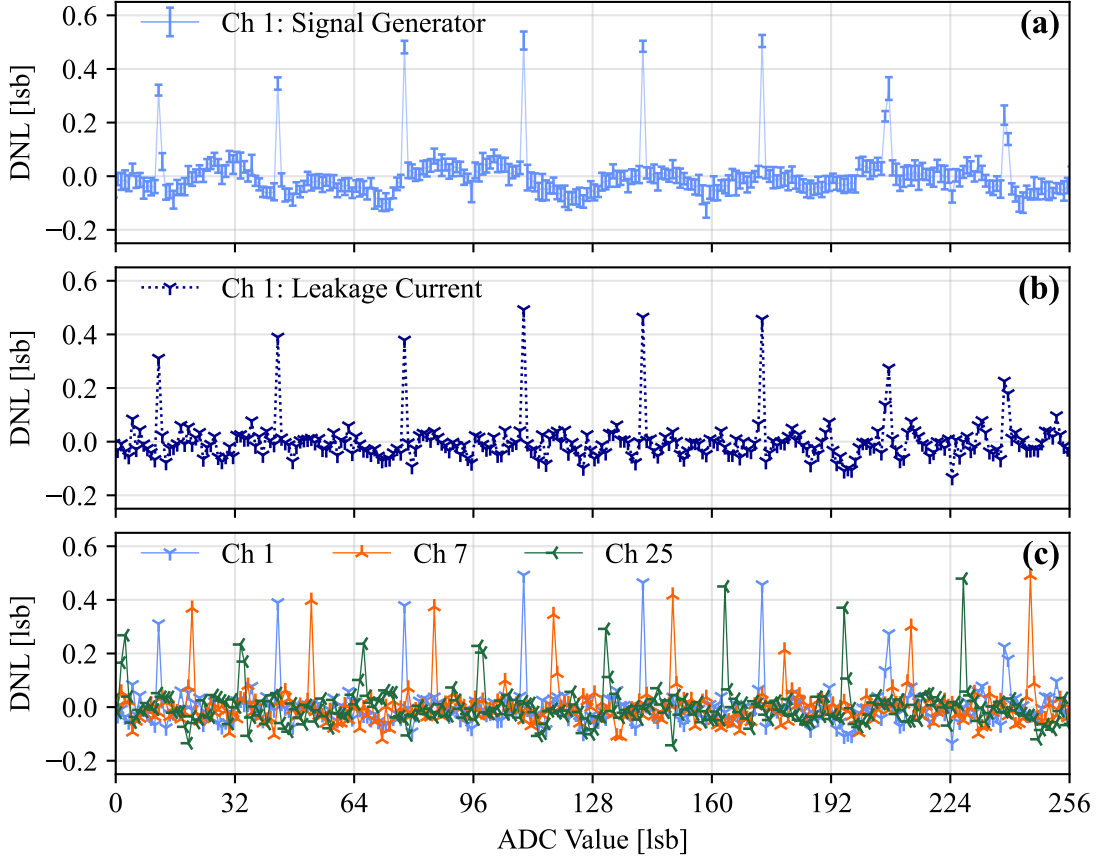


Figure 5. Comparison of the measured differential non-linearity (DNL) for an 8-bit range of the ADC's digitization range. (a) Measured DNL using the UPV Audio Analyzer voltage source with errorbars calculated from ten independent measurements over a four month period. (b) Measurement of the same channel's DNL using the TRISTAN detector leakage current, demonstrating the consistency of the methods. (c) Comparison of the DNL of three ADC readout channels. Ch 1 and 7 are channels on the same ADC card and Ch 25 is from a separate ADC card.

Over a four month period ten measurements of the same readout channels were made with variable voltage slope values and with multiple power cyclings of the DAQ system. The errorbars presented in [Figure 5 \(a\)](#) are the calculated standard deviations of the ten measurements. Over the four months the spacing and location of the comb-like spikes were stable and the background noise

remained consistent with the measured fluctuations and statistical uncertainty. ADC bins directly adjacent to the spikes exhibited small over-fluctuations on the scale of $\approx 3.2\sigma$, which is attributed to a small variability of the peak widths over time.

Although the need for repeated linearity measurements is reduced by the stability of the DNL, an in-situ measurement method was developed and demonstrated. The use of signal generator waveforms becomes prohibitively difficult after the mounting of the TMB onto the detector chamber, and therefore the method utilizes TRISTAN detector signals. The TRISTAN detector has a characteristic leakage current, caused by random charge buildup, which produces a slow linear signal in the first-stage readout. By directly digitizing the first-stage readout for a detector without events occurring, the DNL can be reconstructed in the same method as the slow linear ramp of a signal generator. Measurements were performed with a prototype TRISTAN detector operated at room temperature. The resulting leakage current sourced a slope of -0.059 lsb/sample which was used to accumulate 7.2×10^8 counts to have comparable statistical sensitivity to the previous measurements. The measured DNL of the same channel are compared in [Figure 5 \(a\)](#) and [\(b\)](#) for the signal generator and leakage current measurement methods, respectively. The agreement between the two methods provides validation of the in-situ measurement procedure that can be performed with minimal interference to the operation of the TRISTAN detectors.

Correlations between the DNL of readout channels is important to the modeling of the systematic bias introduced from the non-linearity, as discussed in [Section 6](#). A comparison of the 36 readout channels on five ADC cards indicated consistent performances for all channels but with no correlations between the structure between channels. The calculated DNLs for three channels are compared in [Figure 5 \(c\)](#), showing the independence of the location of the comb-like spikes within the ADC range. Some variability in spike amplitude and additional subdominant spike structures of 4-bit and 6-bit were observed in a few readout channels.

Characterization of the DNL structure of the readout channels of the TMBs installed for the TRISTAN update will be performed before and after installation using the presented methods. The extracted parameters of the population of DNLs is used as an input to directly model the systematic effect of the non-linearity on the measured physics signal of the TRISTAN detector upgrade.

6 Sterile Neutrino Sensitivity

Non-linearities in the DAQ system bias the energy reconstruction of the filter logic presented in [Section 4](#). The systematic effect of this bias influences the ability to perform a high precision measurement of the decay spectrum. A previous study indicated the systematic effect of ADC non-linearities limited a KATRIN-like search for sterile neutrinos to mixing of $\sin^2 \theta > 10^{-5}$ [\[22\]](#). The impact of ADC non-linearities on precision energy reconstruction were also shown in germanium detectors and require mitigation in the MAJORANA DEMONSTRATOR [\[23\]](#). In this work the systematic weakening of sterile neutrino exclusion possible due to the ADC non-linearity systematic is compared to the statistical sensitivity of measuring 10^{15} tritium β -decay electrons. Improved modeling and mitigation strategies were applied in this work to determine the necessary effort to maximize the sensitivity to sterile neutrinos in the TRISTAN measurement phase.

A systematic sensitivity contour is produced by scanning over sterile neutrino parameters from $m_4 = 0$ keV to 17.5 keV, and mixing down to $\sin^2 \theta = 10^{-8}$ [\[24\]](#). At each point the model is

compared with and without the systematic effect, which is parameterized by a covariance matrix. A χ^2 value is calculated at each point from the data-to-model residuals and a 95% C.L. exclusion is drawn at the boundary where $\chi^2 = 5.991$ [25]. For each DAQ operating condition a covariance matrix is constructed by calculating the average bias to the measured spectrum for 1000 DNL structures produced through Monte Carlo simulations using the measured parameters of [Section 5](#).

The resulting sensitivity contours for various operating parameters are presented in [Figure 6](#) and explained in the following sections. In each of the figures the contours are compared to the statistical sensitivity of a measurement of 10^{15} electrons and the previously published systematic limit accounting for ADC non-linearities, labeled Dolde 2017 [22].

The sterile neutrino sensitivity calculated for operation at count rates of 10, 50, and 100 kcps per pixel are shown in [Figure 6](#) (a). While operating at low count rates, the majority of events begin after the previous signal has completely decayed back to the detector operating point. Therefore, events of the same energy deterministically cover the same ADC range and experience the same non-linearity. Increasing the count rate causes events to begin on the still decaying pulse tail of previous events. Therefore, events with the same energy will occur over a distribution of ADC ranges and experience different non-linearities. The averaging of non-linearities experienced for pulses of the same energy smoothens the energy dependence and decreases the amplitude of the distortion to the spectrum. Operation at a per pixel rate of 100 kcps is shown to reduce the systematic effect to nearly recover the projected statistical sensitivity.

The sensitivity for the same count rates is recalculated for a PAE voltage of 20 kV in [Figure 6](#) (b), in comparison to the currently possible 10 kV used in (a). An upgrade to the PAE to enable operation at 20 kV was designed to decrease the probability of back-scattering and pileup in the measured spectrum but is also beneficial to reducing the impact of the non-linearity systematic. An increase of the PAE voltage increases the kinetic energy of the electron before it is incident on the detector. The increased energy of the electrons increases the dynamic range of the digitized waveforms, which also acts to average out the non-linearity experienced by the pulses.

The starting ADC position of pulses can also be artificially changed by applying an analog offset to the detector response before digitization [26]. This distortion reduction behaves similarly to that of increasing count rates, by changing the non-linearity effect experienced by events of the same energy. The voltage offset is applied by the Gatti slider submodule of the TMB to the waveforms before digitization and is communicated to the Serenity-S1 back end processing to be removed before event filtering. An improvement to the sensitivity while operating at a low count rate of 10 kcps per pixel is demonstrated in [Figure 6](#) (c) with the application of an analog Gatti slider with widths of 100 mV and 200 mV, which is equivalent to 819 and 1638 ADC bins. The ability to regain sensitivity while operating at low count rates could be important for measurements that are made to study the impact of other systematic effects.

The previous sensitivity contours were calculated assuming the measurement used a single pixel with an ADC non-linearity parameterized by the calculated covariance matrix. In practice, the spectral measurement will be made with $\mathcal{O}(1000)$ pixels, which introduce further reductions to the ADC non-linearity systematic. If the non-linearities of different ADC channels are uncorrelated, then the spectral distortion for multiple channels are also uncorrelated and can be reduced by averaging spectra from multiple pixels. [Figure 6](#) (d) shows the impact of performing a low rate measurement with a single pixel, a single TRISTAN module, and the designed nine TRISTAN

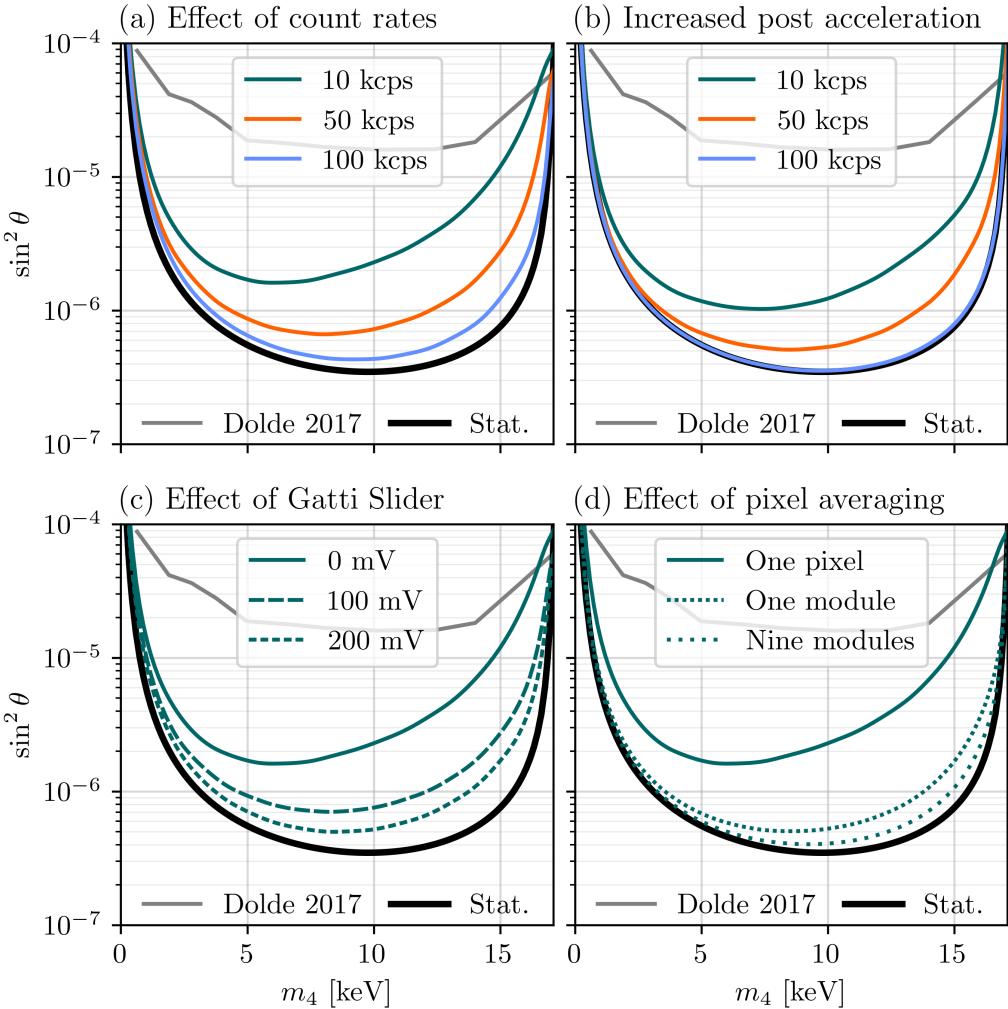


Figure 6. 95% C.L. exclusion contours for sterile neutrino mixing accounting for the ADC non-linearity systematic compared to the statistical sensitivity of measuring 10^{15} electrons. This work improves on the treatment of Dolde 2017, which indicated limitations in sensitivity of $\sin^2 \theta > 10^{-5}$ due to spectral distortions introduced by non-ideal ADC bin widths [22]. A recovery of sensitivity is shown for increasing the detector count rate from 10 kcps to 100 kcps for the case of operating with a 10 kV and 20 kV PAE voltage, in (a) and (b), respectively. For a measurement at 10 kcps, the sensitivity is demonstrated to be improved through the application of a Gatti slider (c) and pixel averaging (d).

modules. The impact of averaging spectra measured from N pixels together shows the overall distortion scaling with $1/\sqrt{N}$. The assumption of uncorrelated channel readouts was validated by the DNL measurement of 36 channels, shown in Figure 5 (c).

Simulations indicate that the combination of any two of the mitigation strategies presented are sufficient to decrease the impact of the ADC non-linearities on the spectrum to below the 10^{-6} level.

The impact of such distortions on the sensitivity of the TRISTAN detector upgrade’s measurement of a sterile neutrino signature becomes a non-dominant systematic. It also demonstrates the ability to maintain the non-dominant systematic impact while operating the detector in various experimental configurations, which can be used in studying the impact of other systematic effects. Sensitivity projections with increased statistics indicate that measurements sensitive to two to three orders of magnitude smaller sterile neutrino mixing are uninhibited by ADC non-linearities.

7 Conclusion

To meet the experimental challenges of operating the TRISTAN detector upgrade to the KATRIN experiment a custom RADC DAQ system is developed that physically separates signal digitization and processing components. The magnetic field and high-voltage compatible front-end TMB is designed to operate and readout the TRISTAN detectors. The Gatti Slider module of the TMB allows for arbitrary waveform offsets before digitization to reduce the impact of non-linearities in the reconstructed event energies.

Flexible digital pulse processing is applied in the Serenity-S1 FPGA cards that make up the back-end. Application of a custom trigger logic, trigger map, and event flagging system allows for accurate energy evaluations and to mitigate event pileup and crosstalk effects. The operational modes of the RADC DAQ system provide a scalable readout of the $O(1000)$ channels with reasonable output datarates for post-processing and analysis.

The first tests of the TRISTAN RADC DAQ system’s linearity are shown to meet the design requirements through two independent measurement methods. The ability to use the detector leakage current as a source for non-linearity measurements demonstrates a mechanism for in-situ characterizations after detector installation. High rate detector operation, an increased PAE voltage, and the operation of an analog Gatti slider enable a reduction of the distortion from ADC non-linearities on the measured differential spectrum. The sensitivity to sterile neutrino mixing for a measurement of 10^{15} electrons is shown to be unimpeded by ADC non-linearities.

Acknowledgments

This material is based upon work supported by the U.S. Department of Energy, Office of Science, Office of Nuclear Physics under Award Numbers DE-FG02-97ER41041, and DE-FG02-97ER41033, and by the National Science Foundation under Grant No. NSF OISE 1743790. This project has received funding from the European Research Council (ERC) under the European Union Horizon 2020 research and innovation programme (grant agreement no. 852845). We acknowledge that we made use of the Serenity-S1 boards developed by the Serenity Collaboration for the high-luminosity upgrade of the CMS experiment at the LHC.

References

- [1] K.N. Abazajian et al., *Light Sterile Neutrinos: A White Paper*, [1204.5379](https://arxiv.org/abs/1204.5379).
- [2] M.A. Acero et al., *White paper on light sterile neutrino searches and related phenomenology*, *Journal of Physics G: Nuclear and Particle Physics* **51** (2024) 120501 [[2203.07323](https://arxiv.org/abs/2203.07323)].

- [3] R. Adhikari et al., *A white paper on kev sterile neutrino dark matter*, *Journal of Cosmology and Astroparticle Physics* **2017** (2017) 025–025 [[1602.04816](#)].
- [4] A. Boyarsky et al., *Sterile neutrino dark matter*, *Progress in Particle and Nuclear Physics* **104** (2019) 1–45 [[1807.07938](#)].
- [5] M. Aker et al., *Direct neutrino-mass measurement with sub-electronvolt sensitivity*, *Nature Phys.* **18** (2022) 160 [[2105.08533](#)].
- [6] M. Aker et al., *Direct neutrino-mass measurement based on 259 days of katrin data*, *Science* **388** (2025) 180–185 [[2406.13516](#)].
- [7] M. Aker et al., *Improved ev-scale sterile-neutrino constraints from the second katrin measurement campaign*, *Physical Review D* **105** (2022) [[2201.11593](#)].
- [8] M. Aker et al., *Search for kev-scale sterile neutrinos with the first katrin data*, *The European Physical Journal C* **83** (2023) 763 [[2207.06337](#)].
- [9] S. Mertens et al., *A novel detector system for katrin to search for kev-scale sterile neutrinos*, *Journal of Physics G: Nuclear and Particle Physics* **46** (2019) 065203 [[1810.06711](#)].
- [10] D. Siegmann et al., *Development of a silicon drift detector array to search for kev-scale sterile neutrinos with the katrin experiment*, *Journal of Physics G: Nuclear and Particle Physics* **51** (2024) 085202 [[2401.14114](#)].
- [11] P. Trigilio et al., *Ettore: a 12-channel front-end asic for sdds with integrated jfet*, in *2018 IEEE Nuclear Science Symposium and Medical Imaging Conference Proceedings (NSS/MIC)*, pp. 1–4, 2018, [DOI](#).
- [12] J. Amsbaugh et al., *Focal-plane detector system for the katrin experiment*, *Nuclear Instruments and Methods in Physics Research Section A: Accelerators, Spectrometers, Detectors and Associated Equipment* **778** (2015) 40–60 [[1404.2925](#)].
- [13] L. Calligaris et al., *A flexible and low-cost open-source ipmc mezzanine for atca boards based on openipmc*, *Journal of Instrumentation* **17** (2022) C03007 [[2112.12888](#)].
- [14] B. Baker, *An699 anti-aliasing, analog filters for data acquisition systems*, Tech. Rep. **1**, Microchip Technology Inc., Chandler, AZ, USA (1999).
- [15] T. Mehner et al., *Serenity-s1 - a versatile atca processing card for the cms phase-2 upgrade*, *techrxiv* (2025) .
- [16] T. Mehner et al., *Lessons learned while developing the serenity-s1 atca card*, *Journal of Instrumentation* **19** (2024) C02018 [[2311.02222](#)].
- [17] J. Mostafa et al., *100-gbit/s udp data acquisition on linux using af_xdp: The tristan detector*, *IEEE Transactions on Nuclear Science* **72** (2025) 295.
- [18] J. Mostafa et al., *Are kernel drivers ready for accelerated packet processing using af_xdp?*, in *2023 IEEE Conference on Network Function Virtualization and Software Defined Networks (NFV-SDN)*, pp. 117–122, 2023, [DOI](#).
- [19] L. Michaeli et al., *Error models of the analog to digital converters*, *Measurement Science Review* **14** (2014) 62.
- [20] T. Linnenbrink et al., *Adc testing with ieee std 1241-2000*, in *IMTC 2001. Proceedings of the 18th IEEE Instrumentation and Measurement Technology Conference. Rediscovering Measurement in the Age of Informatics (Cat. No.01CH 37188)*, vol. 3, pp. 1986–1991 vol.3, 2001, [DOI](#).

- [21] T. Kuyel, *Linearity testing issues of analog to digital converters*, in *International Test Conference 1999. Proceedings (IEEE Cat. No.99CH37034)*, pp. 747–756, 1999, [DOI](#).
- [22] K. Dolde et al., *Impact of adc non-linearities on the sensitivity to sterile kev neutrinos with a katrin-like experiment*, *Nuclear Instruments and Methods in Physics Research Section A: Accelerators, Spectrometers, Detectors and Associated Equipment* **848** (2017) 127–136 [[1608.03158](#)].
- [23] N. Abgrall et al., *Adc nonlinearity correction for the majorana demonstrator*, *IEEE Transactions on Nuclear Science* **68** (2021) 359–367 [[2003.04128](#)].
- [24] S. Mertens et al., *Sensitivity of next-generation tritium beta-decay experiments for kev-scale sterile neutrinos*, *Journal of Cosmology and Astroparticle Physics* **2015** (2015) 020 [[1409.0920](#)].
- [25] S. Mertens et al., *Characterization of silicon drift detectors with electrons for the tristan project*, *Journal of Physics G: Nuclear and Particle Physics* **48** (2020) 015008 [[2007.07136](#)].
- [26] E. Gatti et al., *Improvement of sliding-scale analog-to-digital converters through weighted averaging*, *IEEE Transactions on Nuclear Science* **16** (1969) 10.